Available online at www.sciencedirect.com
SCIENCE DIRECT®
Tectonophysics 376 (2003) 75–97
TECTONOPHYSICS
www.elsevier.com/locate/tecto

Some tectonic consequences of fluid overpressures and seepage forces as demonstrated by sandbox modelling

R. Mourgues, P.R. Cobbold*

Géosciences-Rennes (UMR 6118 du CNRS), Campus de Beaulieu, Universite de Rennes 1, Avenue du General-Leclerc, 35042 Rennes Cedex, France

Received 17 February 2003; accepted 28 July 2003

Abstract

We demonstrate some of the effects of fluid overpressures and seepage forces in tectonics using the results of scaled physical models. According to von Terzaghi's principle, the total state of stress in a saturated porous medium is the sum of an effective stress which controls the deformation and an isotropic fluid pressure. In tectonics, for any variation in pore fluid pressure, it is common to assume that total stresses are constant. Such an assumption is not always warranted. In experiments where air flows through sand packs, we demonstrate that gradients in fluid overpressure cause seepage forces and that these may modify total stresses. Using these principles, we have obtained yield functions for Fontainebleau sand at very small effective stresses (>5 Pa). We have corrected our results and other previously published results for significant effects of sidewall friction. For normal stresses larger than 30 Pa, the sand has a linear Coulomb yield function. The corrected cohesion is much smaller than previously reported. In extensional tests involving vertical fluid flow, the dihedral angle between conjugate normal faults decreases as effective stresses tend to zero. For nonvertical fluid flow, seepage forces modify the principle directions of stress, producing listric faults. In a sloping sedimentary sequence, the dip of normal faults depends on the overpressure gradient. We have also obtained a reorientation of principal stresses in two-dimensional numerical models. By introducing a layer of small permeability, we have been able to induce gravitational gliding in an overpressured sloping sand pack.

Keywords: Fluid overpressures; Seepage forces; Sandbox modelling; Tectonic consequences

1. Introduction

In the 1920s and 1930s, Paul Fillunger and Karl von Terzaghi investigated the mechanical behaviour of saturated porous solids as part of their work on soils and embankments. von Terzaghi (1923) studied consolidation in one dimension. He became famous for having been the first, apparently, to discover the principle of effective stress. Nevertheless, it is clear from the work of Fillunger (1914) that he, too, fully understood this principle (de Boer, 2000). Fillunger investigated the force of uplift on a dam and the frictional drag (now known as seepage force) due to flow of a liquid through a porous medium. He was the first to state clearly that constitutive equations for porous media should not be expressed in terms of total stresses alone.

* Corresponding author. Tel.: +33-223236096; fax: +33-223236100.
E-mail addresses: Regis.Mourgues@univ-rennes1.fr (R. Mourgues), peter.cobbold@univ-rennes1.fr (P.R. Cobbold).

0040-1951/$ - see front matter © 2003 Elsevier B.V. All rights reserved.
doi:10.1016/S0040-1951(03)00348-2

Biot (1941) generalized the theory of von Terzaghi (1923) to three dimensions, providing a basis for many further developments where fluid and deformation are coupled in a feedback manner (Nur and Byerlee, 1971; Garg and Nur, 1973; Robin, 1973; Rice and Cleary, 1976; Strayer et al., 2001). By carrying a part of the total stress, the fluid affects the likelihood of failure in the solid framework. As it flows through pore space, the fluid imparts frictional forces (seepage forces) to the solid framework, thereby modifying the balance of forces. Reciprocally, deformation of the framework modifies the porosity and permeability, so changing the rate of fluid flow. These principles have found their way into several geological fields of application, including seismic pumping (Rice, 1975; Rudnicki, 1984; Sibson, 2000) and topography-driven fluid flow (Oliver, 1986; Garven, 1995).

Hubbert and Rubey (1959) wrote a pioneering article on the importance of pore fluids in tectonic processes. Although the article generated some controversy (Laubsher, 1960; Birch, 1961; Moore, 1961), it has remained a standard reference for structural geologists. Fluid pressures have become fundamental to the mechanics of deltas (Hubbert and Rubey, 1959; Mandl and Crans, 1981) and accretionary thrust wedges (Davis et al., 1983; Dahlen, 1984; Dahlen et al., 1984; Lehner, 1986). At smaller scales, fluids are held to be responsible for hydraulic fracturing (Hubbert and Willis, 1957; Sibson, 2000) and for modifying the shapes of normal faults (Price, 1977; Crans et al., 1980; Mandl and Crans, 1981; Bradshaw and Zoback, 1988).

In the last few decades, analogue modelling has been of great help in understanding tectonic processes at various scales (for historical and thematic reviews, see Koyi, 1997; Cobbold and Castro, 1999). However, the use of pore fluids in such models is relatively new. Cobbold and Castro (1999) showed that it was feasible to use compressed air as a pore fluid in sandbox models, opening the way for other developments. Cobbold et al. (2001) were able to verify some of the theoretical predictions for thrust wedges (Hubbert and Rubey, 1959; Dahlen, 1990), and they showed that permeability is important in controlling the positions of thin-skinned detachments.

In this paper, we use the same experimental technique to demonstrate and verify the role of seepage forces in tectonics. Although the effects of seepage forces are widely understood in soil mechanics, and some tectonic analyses have taken them into account (Crans et al., 1980; Iverson and Major, 1986; Dahlen, 1990; Iverson, 1991; Byerlee, 1992; Iverson and Reid, 1992; Orange and Breen, 1992), on the whole they seem to be little known to geologists. Most standard textbooks on structural geology (e.g. Hobbs et al., 1976; Ramsay and Huber, 1983; Price and Cosgrove, 1990) pay little or no attention to them. Possibly for these reasons, many authors (e.g. Mello and Pratson, 1999; Willis and Buck, 1997) have attempted to calculate effective stresses by first taking total stresses and then subtracting fluid overpressures. With the help of a very simple experiment, we will show that such an approach can easily give the wrong answer. The correct and safe approach is first to consider how fluid flow and resulting seepage forces modify effective stresses, and then to calculate total stresses according to von Terzaghi's principle.

2. Suitable reference surfaces for effective stress

Although the concept of effective stress has now become clear, for many years, it was a source of controversy. According to Mandl (1988) this is understandable, the problem being how to apply the concept of effective stress to different kinds of material.

When considering a porous medium, we need a reference surface in order to define effective stress. Mandl (1988) gives a detailed discussion of the subject, which figured prominently in early theories on porous saturated media (see, for example, Fillunger, 1913). It has also figured in many discussions on the applicability of von Terzaghi's principle, a notorious example being in the aftermath of Hubbert and Rubey's article (Laubsher, 1960; Birch, 1961; Moore, 1961; Dahlen, 1990).

Here, we will consider here only two kinds of reference surface, which are relevant to granular materials (Fig. 1). Surface A_1 is planar and cuts through the solid matrix of a porous medium without regard for position or orientation (Fig. 1a). If Ψ is

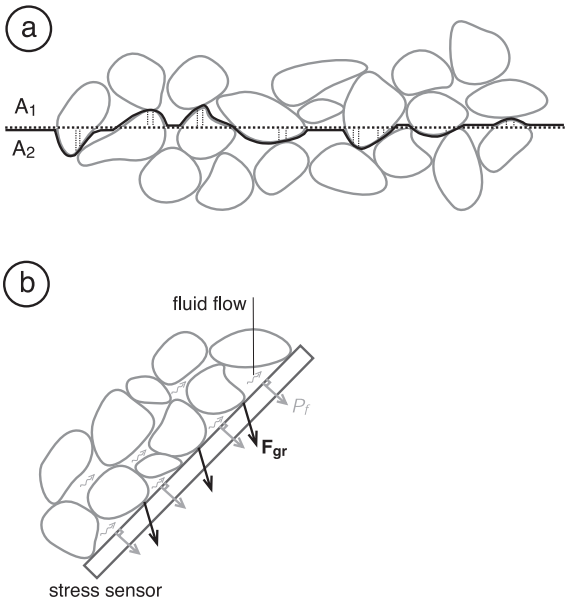

Fig. 1. Reference surfaces for defining effective stress in a saturated porous granular medium. Surface A_1 is planar and cuts across grains and fluid (a). Surface A_2 is undulating and passes through point contacts between grains. Planar surface of stress sensor (b) also is in point contact with grains.

the surface porosity, the total normal stress acting on A_1 is (Table 1):

$$S = S_s + \Psi.P_f \quad (1)$$

Here S is the total normal stress, S_s is the 'normal skeletal stress' per unit area of A_1 and P_f is the pore fluid pressure. The effective normal stress (von Terzaghi, 1923) is then:

$$S' = S - P_f = S_s + (\Psi - 1).P_f \quad (2)$$

Now, consider an undulating surface, A_2, which follows A_1 as closely as possible, but goes through the solid skeleton at intergranular contacts only. We project the fluid part of this undulating surface on A_1, so defining the porosity Ψ_2. The total normal stress is then:

$$S = S_{gr} + \Psi_2.P_f \quad (3)$$

Here, S_{gr} is the 'normal intergranular stress' (stress transmitted across the intergranular contacts of the undulating surface and projected onto A_1).

Table 1
Common symbols and units

$\boldsymbol{\sigma}$	total stress tensor	Pa
$\boldsymbol{\sigma'}$	effective stress tensor	Pa
$\boldsymbol{\delta}$	identity matrix	–
$\boldsymbol{V}$	fluid velocity	m s^{-1}
$\boldsymbol{F_w}$	weight per unit volume	N m^{-3}
$\boldsymbol{F_a}$	buoyancy force per unit volume	N m^{-3}
$\boldsymbol{F_s}$	seepage force per unit volume	N m^{-3}
$\boldsymbol{R}$	resultant body force per unit volume	N m^{-3}
$\boldsymbol{Q}$	Darcy velocity	m s^{-1}
$\boldsymbol{k}$	intrinsic permeability tensor	m^2
τ	shear stress	Pa
σ_n	normal stress	Pa
S_s	normal skeletal stress	Pa
S_{gr}	normal intergranular stress	Pa
P_f	pore fluid pressure	Pa
∇P_{nh}	nonhydrostatic part of the fluid pressure gradient	Pa m^{-1}
P_b	basal fluid pressure	Pa
P_{up}	top fluid pressure	Pa
P_{at}	atmospheric fluid pressure	Pa
dP_f	variation of fluid pressure (in time)	Pa
λ	ratio of pore fluid pressure and vertical stress	–
Ψ	surface porosity	–
Φ	porosity	–
ρ_q	solid density	kg m^3
ρ_s	sand density	kg m^3
ρ_b	bulk density	kg m^3
ρ_w	water density	kg m^3
ν_f	fluid viscosity	Pa s
c	cohesion	Pa
μ	coefficient of internal friction	–
μ_s	coefficient of sliding (sand against wall)	–
ϕ	angle of internal friction	degrees
K	ratio of horizontal to vertical effective stress	–
ν	Poisson's ratio	–
A	surface area	m^2
D	diameter	m
R	radius	m
P	perimeter	m
h	height of sand	m
γ	angle between a fault and the principal compression	degrees
α	slope angle	degrees
ϖ	angle between σ_1' and z-axis	degrees

Should the intergranular contacts become very small ('point' contacts), the porosity Ψ_2 will tend to unity and the intergranular stress S_{gr} will coincide with the effective stress, which acquires a simple mechanical meaning:

$$S' = S - P_f = S_{gr} \quad (\Psi = 1) \tag{4}$$

In a granular medium with point contacts where deformation is by relative motion between the grains, intergranular stresses (S_{gr}) transmit from one grain to another and the reference surface A_2 is equivalent to the flat face of a stress sensor (Fig. 1b). Many experiments have confirmed that the effective stresses of Eq. (4) control deformation in such a medium. More surprisingly, perhaps, this control also applies to a variety of rocks having large intergranular contacts and even to rocks where the matrix has no granular structure at all (Handin et al., 1963; Hubbert and Rubey, 1959; Mandl, 1988).

3. Forces exerted by a nonhydrostatic gradient of fluid pressure on a porous medium

A nonhydrostatic gradient of pore fluid pressure causes fluid to flow through a porous medium, provided that fluid viscosity is small enough and permeability of the medium is large enough. Under these conditions, the seeping fluid transmits forces to every grain.

The constitutive law for a Newtonian fluid with constant viscosity is:

$$\sigma_{ij}(M,t) = P_f(M,t)\delta_{ij} + v_f(\partial V_i/\partial x_j + \partial V_j/\partial x_i) \tag{5}$$

Here, $\sigma_{ij}(M,t)$ are Cartesian components of the stress tensor at point M and time t, P_f is fluid pressure, δ_{ij} are components of the unit tensor, v_f is fluid viscosity, V_i are Cartesian components of the

Table 2
Viscous forces in a granular medium
By following two approaches to the calculation of effective stresses, we can estimate the viscous forces in a saturated granular medium with or without fluid flow. We assume point contacts between grains

Continuous medium approach	Granular medium
A porous medium is subject to gravity. In two dimensions, the equations of state are: $\partial\sigma_{xx}/\partial x + \partial\sigma_{xz}/\partial z = 0$ $\partial\sigma_{zx}/\partial x + \partial\sigma_{zz}/\partial z = \rho_b g$ where ρ_b is the bulk density, and z is positive downwards. By introducing effective stresses, $\sigma'_{xx} = \sigma_{xx} - P_f$, $\sigma'_{zz} = \sigma_{zz} - P_f$ and $\sigma'_{xz} = \sigma_{xz}$, we obtain: $\partial\sigma'_{xx}/\partial x + \partial\sigma'_{xz}/\partial z = 0$ $\partial\sigma'_{zx}/\partial x + \partial\sigma'_{zz}/\partial z = \rho_b g - \partial P_f/\partial z$ (a) Fluid in hydrostatic state: $\partial P_f/\partial z = \rho_w g$ Here, assuming variation along z only: $\sigma'_{zz} = \rho_b gz - \rho_w gz = (1-\Phi)(\rho_q - \rho_w)gz$ where ρ_q and ρ_w are the density of the solid and the fluid. (b) Fluid under overpressure, undergoing vertical flow: $\partial P_f/\partial z = \rho_w g + [\partial P_f/\partial z]_{nh}$ Assuming variation along z only: $\sigma'_{zz} = \rho_b gz - \rho_w gz - [\partial P_f/\partial z]_{nh} z$ $= (1-\Phi)(\rho_q - \rho_w)gz - [\partial P_f/\partial z]_{nh} z$	(a) Fluid in hydrostatic state: $\partial P_f/\partial z = \rho_w g$ A grain of arbitrary shape, exterior surface A, and volume V, is immersed in water. The force exerted by the liquid on the solid is: $F = -\int\int P_f dA = -\int\int\int \partial P_f/\partial z dV = -\rho_w g V$ This is the well-known Archimedes force. By assuming that the granular medium is an aggregate of grains with point contacts, each particle will be subjected to this force. The effective vertical stress on a horizontal plane at depth z is: $\sigma'_{zz} = (1-\Phi)(\rho_q - \rho_w)gz$ (b) Vertical water flow: $\partial P_f/\partial z = \rho_w g + [\partial P_f/\partial z]_{nh}$ By neglecting the viscous forces exerted by fluid flow, and by assuming purely horizontal fluid isobars between grains, each particle is subject to a force similar to the Archimedes force. The effective vertical stress is then: $\sigma'_{zz} = (1-\Phi)(\rho_q - \rho_w)gz - (1-\Phi)[\partial P_f/\partial z]_{nh} z$ This result differs from the one obtained with the continuum approach. We can consider the difference $\Phi[\partial P_f/\partial z]_{nh} z$ as an approximation of the viscous force within the granular medium.

fluid velocity vector, and we use the summation convention for repeated Cartesian suffixes.

During laminar flow, two kinds of stresses act on a plane surface A: a normal stress, P_f, and a viscous shear stress, $v_f(\partial V_i/\partial x_j)$. Such stresses, therefore, act on each grain of the solid medium as fluid flows through the pore space. At the grain scale, the effect of normal pressure is easy to understand. Viscous forces are difficult to calculate because of the microscopic complexity of the flow between each grain. Nevertheless, we can define them by considering the porous saturated medium in two different ways (Table 2).

In terms of effective stresses, the equations of state are (Table 2):

$$\partial\sigma'_{xx}/\partial x + \partial\sigma'_{xz}/\partial z = -[\partial P_f/\partial x]_{nh} \quad (6)$$

$$\partial\sigma'_{zx}/\partial x + \partial\sigma'_{zz}/\partial z = (1-\Phi)(\rho_q - \rho_w)g - [\partial P_f/\partial z]_{nh} \quad (7)$$

Here, $[\partial P_f/\partial \ldots]_{nh} = \nabla P_{nh}$ is the nonhydrostatic part of the fluid pressure gradient (or head gradient) which can be an overpressure or an underpressure gradient. The forces acting on each element of solid matrix are (1) its weight, $F_w=(1-\Phi)\rho_q g$, (2) a buoyancy force, $F_a=-(1-\Phi)\rho_w g$ and (3) a seepage force, $F_s=-\nabla P_{nh}$. Although the first two forces act vertically, the third one may act in any orientation, so modifying the principal values and orientations of the effective stresses (Fig. 2).

Despite its name, the seepage force does not depend on fluid velocity through the porous medium, but only on the gradient of fluid pressure. For a given pressure gradient, each grain will be subject to an invariant seepage force no matter what the values of permeability or fluid viscosity are.

To demonstrate these principles, we will describe a series of simple experiments on Fontainebleau sand. In all of them, the pore fluid is compressed air. Buoyancy forces are, therefore, negligible and $\nabla P_f = \nabla P_{nh}$. Although air is compressible, we calculate pore fluid pressures in the sand using Darcy's law, which appears to hold well (Cobbold and Castro, 1999):

$$Q = -(k/v_f)\nabla P_{nh} \quad (8)$$

Here, Q is the Darcy velocity (in m s^{-1}), k is the intrinsic permeability of the sand (in m^2) and v_f is the fluid viscosity (in Pa s).

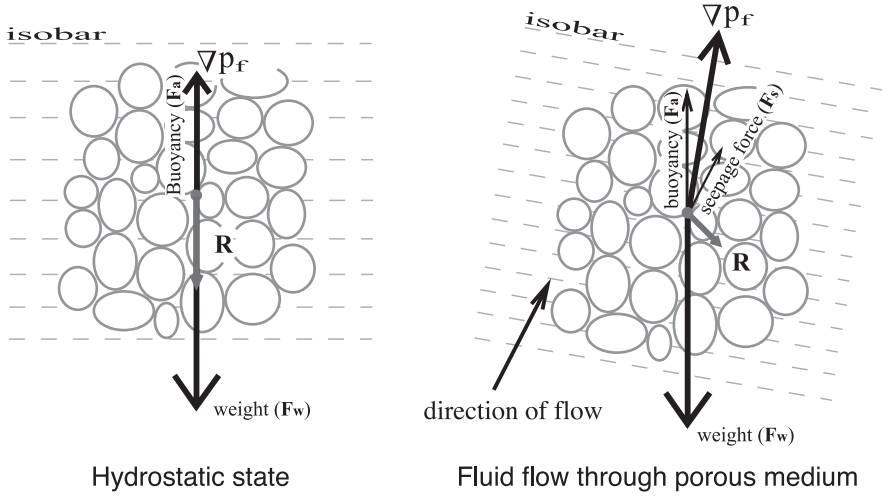

Fig. 2. Forces imparted to grains by a pore fluid. If fluid is in hydrostatic state (left), forces are weight (F_w) and buoyancy (F_a). If there is a gradient of overpressure (right), fluid flows through pore space, imparting additional seepage force (F_s).

4. Experiments involving vertical seepage forces

4.1. Apparent loss (or gain) of weight due to seepage forces

A very simple way of demonstrating seepage forces is to force air vertically through a sand pack while measuring the apparent weight of the sand with a balance.

The operator places a known mass of sand in a cylindrical plastic container (Fig. 3). The cylinder should hang from a support, just touching a sieve that lies on the balance. The sieve allows air to flow through the sand pack, either upwards or downwards. At the top of the container is a system for suction or injection of air. Thus, the fluid pressure, P_f, may be either smaller or greater than atmospheric pressure. On decreasing or increasing the pressure, the operator will notice an apparent loss or gain of weight in the sand. Taking into account inevitable sidewall friction between sand and container, the operator can verify that the apparent weight of the sand equals its true weight, less a factor of $\Delta P_f A$, where A is the cross-sectional area of the container, and $\Delta P_f = P_{at} - P_f$ is the overpressure. Thus, two forces act on the sample: its own weight and $\Delta P_f A$. If $\Delta P_f > 0$ (suction at the top), the weight of the sample apparently decreases; whereas, if $\Delta P_f < 0$ (injection at the top), it increases.

Although the result of this experiment is obvious for an impermeable medium, it is perhaps less intuitive for a permeable medium such as sand.

A simple model of tubular pore space, by providing an exact solution to the equations of viscous flow, demonstrates the action of seepage forces in an analytical way. Consider a disc of solid material within a piston (Fig. 4). Assume no sidewall friction between solid and piston and no fluid flow at the joint. At the base of the solid, the air pressure (P_b) is greater than atmospheric, whereas at the top it is atmospheric (P_{at}).

If the solid is impermeable (Fig. 4a), the upthrust of the liquid upon the solid is simply:

$$P_b A - P_{at} A = \Delta P_f A$$

If the solid is permeable, the upthrust results from viscous forces acting at the base and top, but also within the pores. Consider a porous solid that contains n vertical tubes of radius R. The surface porosity is then:

$$\Psi = n\pi R^2 / A$$

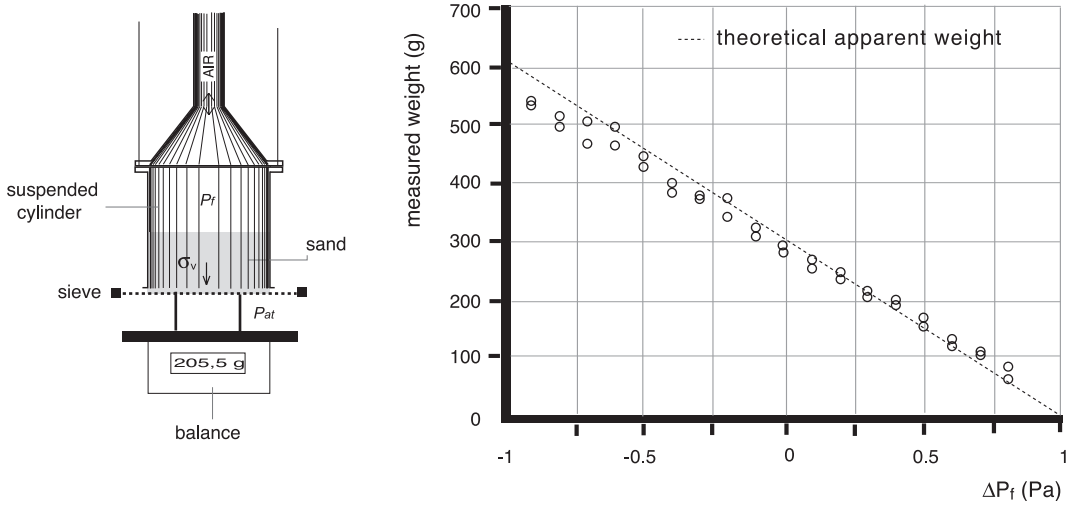

Fig. 3. Apparent loss or gain in weight of a sand pack due to fluid flow. Sand pack lies within suspended cylinder and rests on sieve (left). Air beneath sieve is at atmospheric pressure, whereas air above sand is either underpressured or overpressured. Air, therefore, flows through sand either upward or downward. Apparent weight of sand, as recorded by balance, depends linearly on applied pressure difference as a result of seepage forces (right). True weight of sand is 300 g. Results have been corrected for sidewall friction in cylinder (see text).

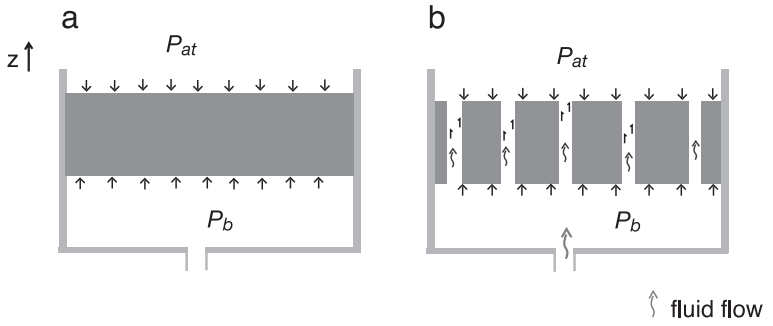

Fig. 4. Effect of differences in fluid pressure across an impermeable solid (a) or a permeable solid containing tubular pores (b).

The lower and upper surfaces are subject to fluid pressure and the forces upon them are $(1-\Psi)P_bA$ and $(1-\Psi)P_{at}A$, respectively. The resultant is, therefore, $(1-\Psi)\Delta P_f A=(A-n\pi R^2)\Delta P_f$.

For fluid flow in the tubes, we take Poiseuille's solution:

$$u(r)=(\partial P_f/\partial z)(r^2-R^2)/(4v_f)$$

Here, $u(r)$ is the vertical velocity of the fluid at a distance r from the axis of the tube and v_f is the viscosity of the fluid.

On the wall of each tube, this flow produces a vertical shear stress, $\sigma_{rz}=v_f\partial u/\partial r=(\partial P_f/\partial z)R/(2v_f)$, where we have assumed that the pressure gradient is constant. By integration of the shear stress over the entire surface of the tube, the vertical force acting on it is $\pi R^2\Delta P_f$.

The total vertical fluid force on the permeable solid is then:

$$F=(A-n\pi R^2)\Delta P_f+n\pi R^2\Delta P_f=\Delta P_f A$$

This simple model shows that the fluid exerts the same vertical force, no matter what the permeability of the medium is. Permeability influences only the nature of the stress (fluid pressure or shear stress) and the way it is distributed (on external or internal surfaces).

The above analysis is enough to show that seepage forces act everywhere, provided that fluid pressures are abnormal. For example, sediment of very small permeability (10^{-15} to 10^{-18} m^2), under a fluid pressure gradient that is close to lithostatic, is subject to a seepage force of the same order of magnitude as its own weight, even though under those conditions and according to Darcy's law, the rate of fluid flow does not exceed 1 mm/year.

4.2. Shear tests

To measure the shear strength of a sand pack during fluid flow, we have done a series of tests with an apparatus (Fig. 5a) that is similar to that of Cobbold and Castro (1999), but has one important modification. In the apparatus of Cobbold and Castro, air pressure was atmospheric above the sample and greater than atmospheric beneath it. As a result, pressure in the shear zone was greater than atmospheric, so that air and sand tended to escape through the narrow space between the two cylinders, especially at the highest pressures. To avoid this problem, we have provided for injection or suction at the top of the sand, as well as at its base, in the manner described previously. By a suitable choice of pressures, air flows through the sand (either upward or downward), while pressure in the shear zone remains atmospheric. Under these conditions, we verify that air and sand no longer escape through the space between the cylinders.

Assuming a constant pressure gradient in the sand, the effective normal stress in the shear zone is, according to Eq. (7):

$$\sigma'_{zz}=(1-\Phi)\rho_q gz-(\partial P_f/\partial z)z=\rho_s gz-(P_b-P_{up})$$

$$=\rho_s gz-\Delta P_f$$

The reader, who prefers to calculate total stress before appealing to von Terzaghi's principle, should be aware that total stress is not simply equal to $\rho_s gz$, but depends also on the air pressure:

$$\sigma_{zz}=\rho_s gz+P_{up}$$

$$\sigma'_{zz}=\sigma_{zz}-P_f(z)=\rho_s gz+P_{up}-P_b=\rho_s gz-\Delta P_f$$

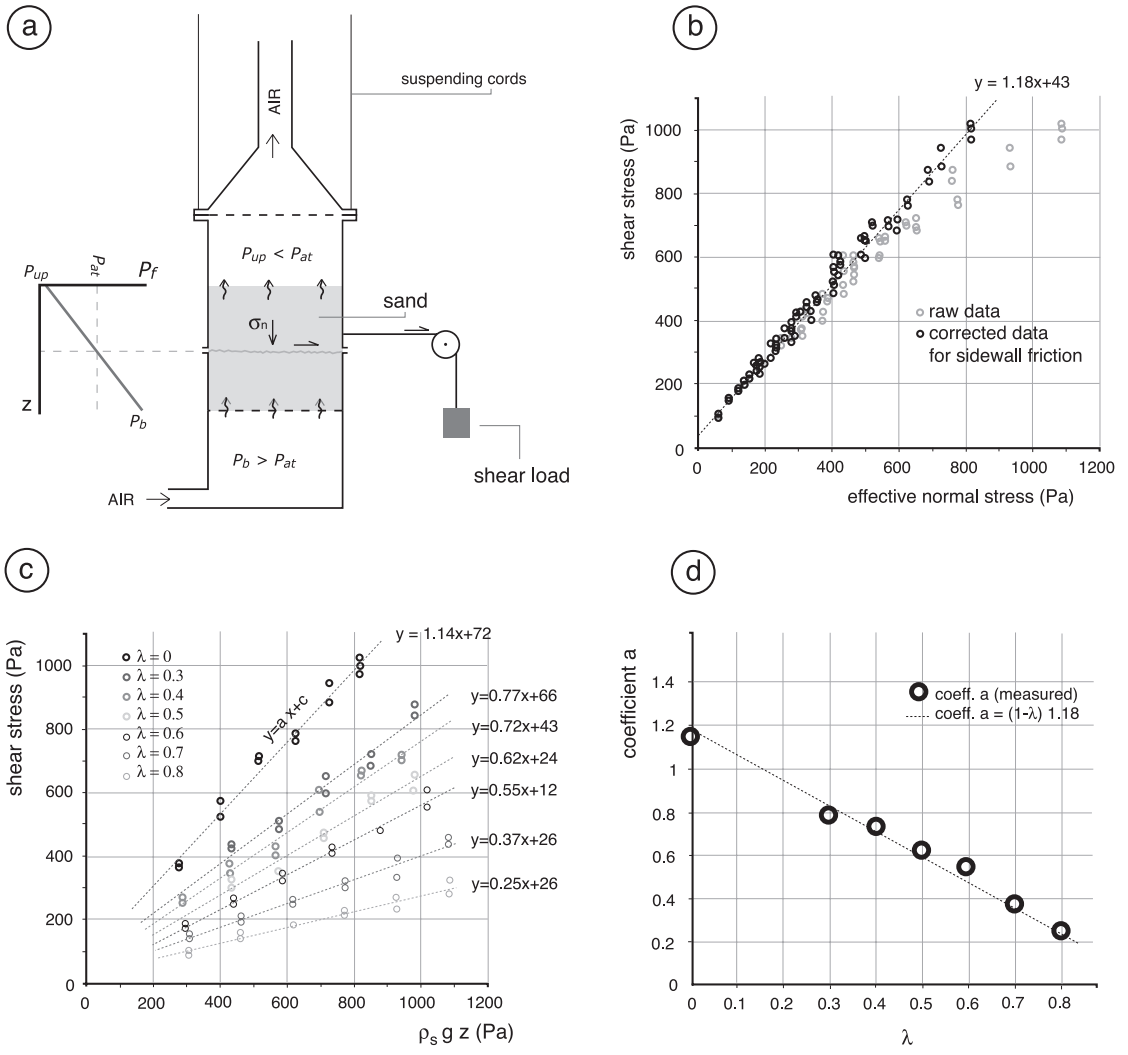

Fig. 5. Shear tests. Apparatus consists of two cylinders (a). Upper cylinder slides to right, under shear load, whereas lower cylinder is fixed. Sand rests on sieve, above lower pressure chamber. Air flows vertically through sand, either upward or downward, according to air pressures in upper chamber (P_{up}) and lower chamber (P_{inf}). By a suitable choice of pressure in chambers, air between cylinders is at atmospheric pressure (P_{at}) and does not leak. For no fluid flow, plot of shear stress versus effective normal stress suggests curved yield envelope for raw data (uncorrected for sidewall friction), but linear envelope for corrected data (b). Notice small value of cohesion (43 Pa) and large coefficient of internal friction (1.18). For fluid flow at various pressure ratios (λ), plot of shear stress versus effective normal stress also suggests linear relationship (c). Slope of lines (a) is linear function of λ, indicating that yield envelope is linear (d). For further explanation, see text.

We now introduce a pressure ratio, λ, which is slightly different from that of Hubbert and Rubey (1959), but identical to that of Cobbold and Castro (1999):

$$\lambda = (P_f(z) - P_{up})/\rho_s g z \quad (9)$$

If $\partial P_f/\partial z$ is invariant with z, λ becomes:

$$\lambda = (\partial P_f/\partial z)/\rho_s g \quad (10)$$

As λ tends to unity, the sand becomes fluidised. Notice also that λ can be negative, implying down-

ward fluid flow. In the shear zone, the vertical effective stress is:

$$\sigma'_{zz} = (1-\lambda)\rho_s g z$$

This expression takes no account of sidewall friction. As in a silo, sidewall friction may partly counteract the weight of the sand (Duran, 1997). The estimated value of vertical effective stress is, therefore, subject to error. As a result, the yield envelope is incorrect. Apparent cohesion is too large, internal friction is too small, and the yield envelope curves more than it should (Appendix A). The results of Krantz (1991), Cobbold and Castro (1999) and Schellart (2000) almost certainly include such undesirable consequences of sidewall friction. To circumvent them, we have used a standard correction due to Jansen (Appendix A).

In our experiments, we sheared sand packs of several thicknesses (2–7 cm) involving different fluid pressures ($\lambda = 0$–0.8). The effective stress on the shear plane ranged from 62 to 820 Pa. To prepare samples with reproducible properties, we first fluidised them and then re-compacted them by tapping at the base of the container (Cobbold and Castro, 1999). The density of the sand was, thus, close to 1600 kg m^{-3}.

On a plot of shear stress as a function of effective normal stress, the data provide a better fit to a straight line after they have been corrected for the silo effect (Fig. 5b). The best-fit straight line is then given by $\tau' = 1.18\sigma'_n + 43$ Pa. For each λ value, we can also fit a straight line to a plot of shear stress versus $\rho_s g z$ (Fig. 5c). We can then plot its slope, a, as a function of λ (Fig. 5d). For $\lambda = 0$, $a = 1.13$, a value that is close to 1.18. Moreover a straight line, $a = 1.18\ (1-\lambda)$, fits the data well. We infer that the Mohr–Coulomb failure envelope, in terms of effective stresses, is:

$$\tau' = c + \mu(1-\lambda)\rho_s g z \qquad (11)$$

Here, $\mu = 1.18$ is the coefficient of internal friction and c is the cohesion.

The latter ranges in value from 12 to 72 Pa (Fig. 5c). The highest values correspond to the greatest sidewall friction (silo effect).

4.3. Extensional tests

For a linear failure envelope, the angle γ between a fault and the principal compression is a simple function of the angle of internal friction, ϕ:

$$\gamma = 45 - \phi/2 \qquad (12)$$

The coefficient of internal friction is $\mu = \tan\phi$. Hence, by measuring the dihedral angle, 2γ, between two conjugate normal faults in a sand model, we can estimate the coefficient of internal friction of the material. For this purpose, we built rectangular sand packs, 30 cm long, 20 cm wide and 4 cm deep, resting on two overlapping sieves. Beneath the sieves was a pressure chamber, which acted as a reservoir for compressed air and provided a uniform fluid pressure at the base of the model (Fig. 6a). To build the packs, we sifted sands of different colours through a sieve (0.5 mm mesh). This handling technique produced a relatively dense pack ($\rho_s = 1700$ kg m^{-3}). By slowly moving one of the sieves, we created a velocity discontinuity at the base of the model. Conjugate normal faults formed at the discontinuity. Extension was just enough to generate fault scarps at the surface, defining a rift valley. However, instead of measuring fault dips at the surface, as did Krantz (1991) and Schellart (2000), we wetted the sand and cut it, so obtaining relatively precise measurements of the angle, ϕ, between conjugate faults (Fig. 6b). We repeated these tests for various rates of flow through the sand.

We assume that (1) the principal effective stress, σ'_1, is vertical and has a value of $(1-\lambda)\rho_s g z$; (2) at yield, the material satisfies a Coulomb criterion, $\tau' = \mu\sigma'_D$; and (3) cohesion is negligible (so that we overestimate the normal stress). From the second and third assumptions, the ratio of principal effective stresses is:

$$\sigma'_1/\sigma'_3 = (1+\sin\phi)/(1-\sin\phi) \qquad (13)$$

The effective normal stress on the fault is:

$$\sigma'_n = (\sigma'_1 + \sigma'_3)/2 - ((\sigma'_1 - \sigma'_3)/2)\sin\phi \qquad (14)$$

From these relationships, we calculate the value of σ'_n at a point half way up the sand. For a nonlinear yield function, $\tau' = f(\sigma'_n)$, the function $\mu = f(\sigma'_n)$ can

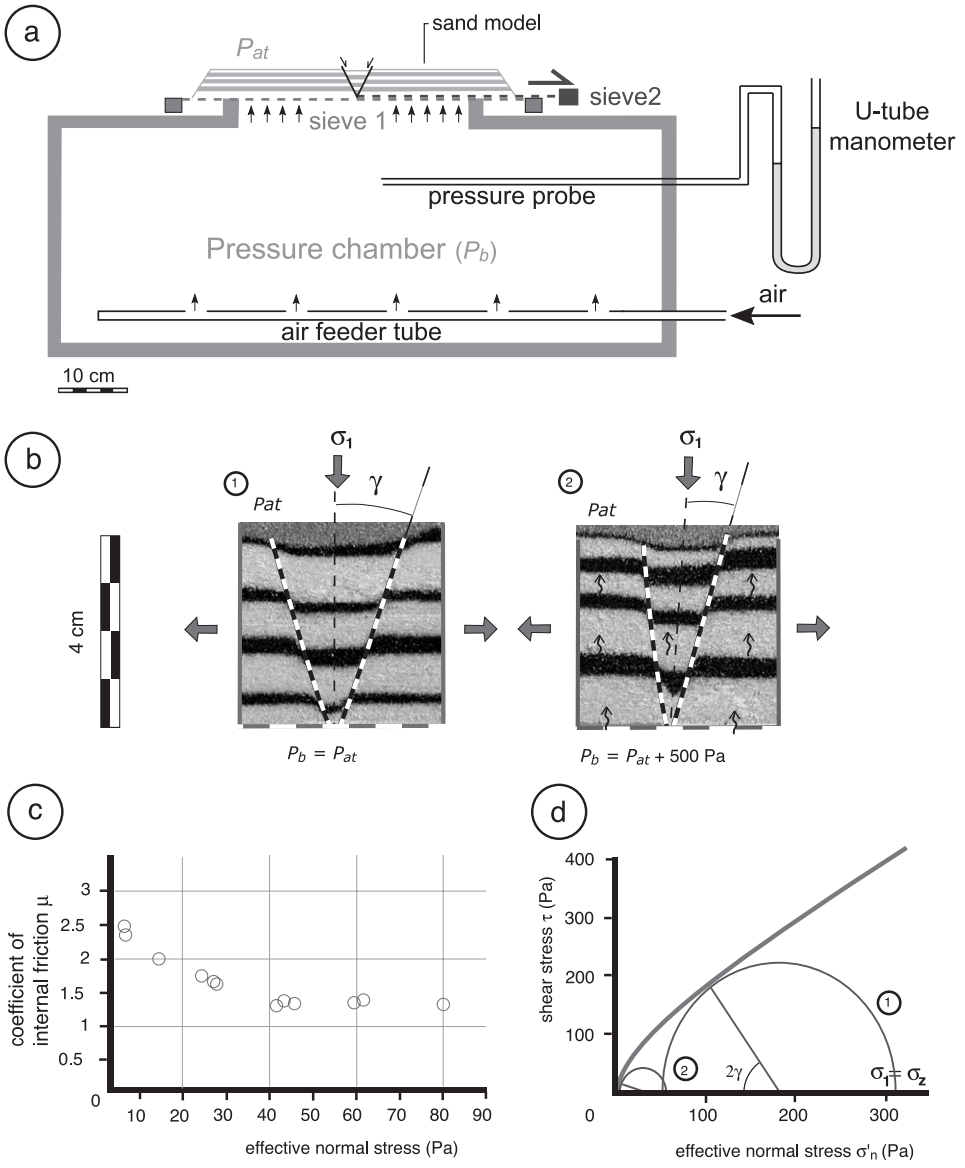

Fig. 6. Decrease in dihedral angle between conjugate faults for small effective stresses. Apparatus (a) consists of two sieves overlapping above centre of pressure chamber. Sand pack rests on sieves. Air flows vertically upwards through sieves and sand. Extensional faults form above velocity discontinuity between sliding sieves. Dihedral angle between conjugate faults decreases as overpressure increases (b). Inferred coefficient of internal friction is large for small effective normal stresses, but decreases to nearly constant value for large effective normal stresses (c). This implies that yield envelope is curved near the origin, but linear away from it (d).

be considered as the first derivative (tangent to the curve). For a linear yield envelope, μ should be constant. On a plot of μ versus σ'_n (Fig. 6c), for values of effective normal stresses greater than 30 Pa, μ is indeed nearly constant, ranging between 1.3 and 1.4. These values of μ are slightly greater than those determined in our shear tests, but they are close to the values determined by Krantz (1991) and Schellart (2000), provided we correct those for sidewall friction. The relatively large values of μ in our exten-

sional tests may have arisen because the sand was denser than it was in the shear tests. For normal stresses smaller than 30 Pa, μ increases, reaching a maximal value of 2.5 (Fig. 6c), which indicates curvature of the yield envelope near the origin. The range of normal stress, over which this curvature occurs, is equivalent to the weight of no more than three or four sand grains. At such a small scale, electrostatic attraction between grains may be responsible for an increase in aggregate strength.

5. Effect of nonvertical seepage forces on stress orientation

5.1. Inclined sedimentary sequence with uniform overpressure at the base

To demonstrate the effect of seepage forces on stress orientation, we will follow Hubbert and Rubey (1959) and Mandl and Crans (1981) in considering an inclined sedimentary sequence with uniform overpressure at the base.

The resultant body force, R, acting on each particle has two components, F_w and F_s (Fig. 7a). The weight, F_w, acts vertically, whereas the seepage force, F_s, is assumed to be perpendicular to the slope. The intensity and orientation of R depend on the relative magnitude of the two components.

5.1.1. Uniform gradient of fluid pressure

We used the same apparatus as described previously (Fig. 6), but inclined it through a few degrees. The sand models were 4 cm thick and 40 cm long. The reservoir provided a constant air pressure (P_b) at the base of the model. Air flowed through the sand in a direction perpendicular to the slope.

As before, conjugate normal faults formed at the velocity discontinuity between overlapping sieves (Fig. 7b). We assume that, at yield, the principal effective compressive stress (σ_1') bisects the dihedral angle between conjugate normal faults. For $P_b = P_{at}$, σ_1' is nearly vertical. For increasing positive values of P_b (indicating overpressure), air flows upward through the sand and the angle between σ_1' and the slope diminishes, so much so that one of the conjugate faults becomes technically a reverse fault. In contrast, for increasing negative values of P_b (underpressure), air flows downward through the sand and the angle between σ_1' and the slope increases until it becomes nearly a right angle. These observations are readily explained in terms of the components of body force.

To analyse the reorientation of the principal stresses as a consequence of seepage forces, we use equations of state in terms of effective stress. Reference axes are parallel and perpendicular to the slope, z being positive downwards:

$$\partial\sigma'_{xx}/\partial x + \partial\sigma'_{xz}/\partial z = \rho_s g\sin\alpha$$

$$\partial\sigma'_{zx}/\partial x + \partial\sigma'_{zz}/\partial z = \rho_s g\cos\alpha - [\partial P_f/\partial z]_{nh}$$

As the slope is infinite, we assume that $\partial\sigma'_{xx}/\partial x = \partial\sigma'_{zx}/\partial x = 0$. The permeability is constant, so that $[\partial P_f/\partial z]_{nh}$ is also constant. The equations simplify to:

$$\sigma'_{xz} = \rho_s g z\sin\alpha$$

$$\sigma'_{zz} = \rho_s g z\cos\alpha - \Delta P_f$$

Here, $\Delta P_f = P_f(z) - P_{at}$.

In terms of principal values, the effective stresses σ'_{xx}, σ'_{zz} and σ'_{xz} are:

$$\sigma'_{zz} = (\sigma'_1 + \sigma'_3)/2 + ((\sigma'_1 - \sigma'_3)/2)\cos(2\varpi) \quad (15)$$

$$\sigma'_{xz} = ((\sigma'_1 - \sigma'_3)/2)\sin(2\varpi) \quad (16)$$

Here, ϖ is the angle between σ_1' and z.

At yield, we assume a Coulomb criterion for effective stress: $\tau' = \mu\sigma'_n$ where $\mu = \tan\phi$. Therefore, we obtain:

$$\sigma'_3 = (1 - \sin\phi)/(1 + \sin\phi)\sigma'_1 \quad (17)$$

For a given value of ΔP_f, we can find values of σ_1', σ_3' and ϖ which satisfy the system of Eqs. (15)–(17) at a depth z. As $[\partial P_f/\partial z]_{nh}$ is constant in depth, so is ϖ. For the purposes of this analysis, we define λ as:

$$\lambda = (P_f(z) - P_{at})/\rho_s g z\cos\alpha$$

We have plotted theoretical curves of ϖ as a function of λ for different values of μ (Fig. 7c). The experimental data are on the same diagram.

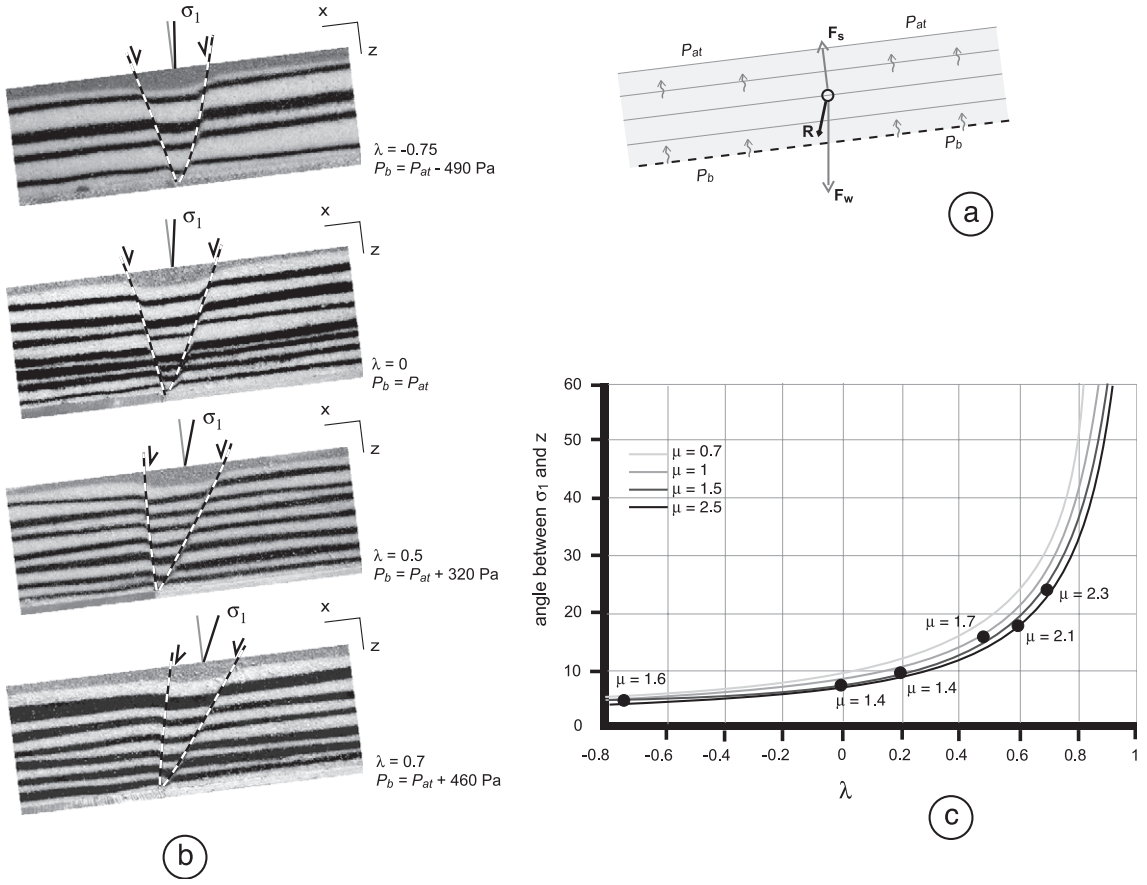

Fig. 7. Reorientations of principal stresses and conjugate extensional faults as a function of overpressure gradient. For apparatus, see Fig. 6a. Conjugate extensional faults form above velocity discontinuity between sliding sieves (b). Assuming that principal compression bisects dihedral angle between conjugate faults, angle between compression and z increases as a function of increasing pressure ratio, λ (c). This is due to increasing contribution of seepage force, F_s, to resultant body force, R (a).

For each experiment, μ was determined by measuring the angle between the two faults. Notice the good agreement between experimental points and theoretical curves. For small gradients of fluid pressure ($\lambda < 0.5$), the points fall between the curves for $\mu = 1.5$ and 1, which are approximately the measured values of μ. As λ increases, the dihedral angle between faults decreases and the points fall closer to curves for $\mu = 1.5$ and 2.5.

Reorientation of principal stresses is a predictable consequence of seepage forces. To calculate total stresses without considering fluid flow, and then to subtract a fluid overpressure from all normal components of the stress tensor, would lead to an erroneous result, in which principal directions are independent of fluid pressure:

$$\tan 2\varpi = -2\sigma_{xz}/((\sigma_{xx} - P_f) - (\sigma_{zz} - P_f)) = -2\sigma_{xz}/(\sigma_{xx} - \sigma_{zz}) \quad (18)$$

Such an error results from an implicit assumption that total stress is invariant, whereas in fact it depends on seepage forces.

5.1.2. Variable gradient of fluid pressure

In the previous experiments, permeability was uniform. In nature, however, permeability commonly

varies with depth (Fig. 8a). In a sedimentary sequence, fluid overpressure tends to build up and survive beneath layers of small permeability (for example, shale), which act as confining layers or dynamic seals. Such layers produce kinks in pressure profiles. Typically, a profile has three main parts. Above a depth Z_a, pore fluid is in a hydrostatic state, so that the profile is steep. Beneath it, a rapid increase in pore pressure results from a confining layer of small permeability, so that the profile is much less steep. Finally, pore fluid maintains a nearly lithostatic pressure.

Such a nonlinear profile has major mechanical effects (Crans et al.,1980; Mandl and Crans, 1981).

1. Principal directions of stress change with depth and so do the dips of resulting faults. For example, assume that a sedimentary sequence dips at a few degrees (say, 5°). For a given angle of internal friction (say, 30°), we may calculate at each depth the principal directions of stress and, therefore, the dips of resulting faults (Fig. 8b). Through-going faults appear listric.
2. At a depth Z_d, the angle between the principle effective stress σ_1' and z reaches as much as 60°. The failure criterion then holds for a plane parallel to bedding, which can act as a detachment for the entire sedimentary sequence.

We have reproduced such a detachment by sandbox modelling (Fig. 9). To obtain a nonlinear profile of pore fluid pressure, we used two grades of sand. The first grade was coarse (315–400 μm) and had a permeability of about 100 Darcy, whereas the second grade was fine (<200 μm) and had a permeability of about 25 Darcy. Models were housed in a rectangular box (40 cm wide by 60 cm long), the bottom being a sieve. A pressure chamber (20 cm wide by 30 cm long) was centred under the model. In this reservoir, the air pressure was initially atmospheric. The internal structure of the models was simple (Fig. 9b). Above a first layer of coarse sand, 1 cm thick, we deposited a second confining layer of fine sand, also 1 cm thick. Finally, we deposited a third layer of coarse sand, 2 cm thick. We tilted the apparatus through 11° and slowly increased the air pressure (P_b). At this stage, the area of sand immediately above the pressure chamber suddenly slid, whereas adjacent areas remained fixed. The central part of the slide remained relatively rigid, whereas the edges deformed. A linear belt of extensional faults formed at the upper edge, a curved thrust belt formed at the lower edge, and overstepping wrench faults formed at each side (Fig. 9a). Within the extensional belt, a rift valley developed. As fast as it subsided, we filled it with coarse sand, so as to

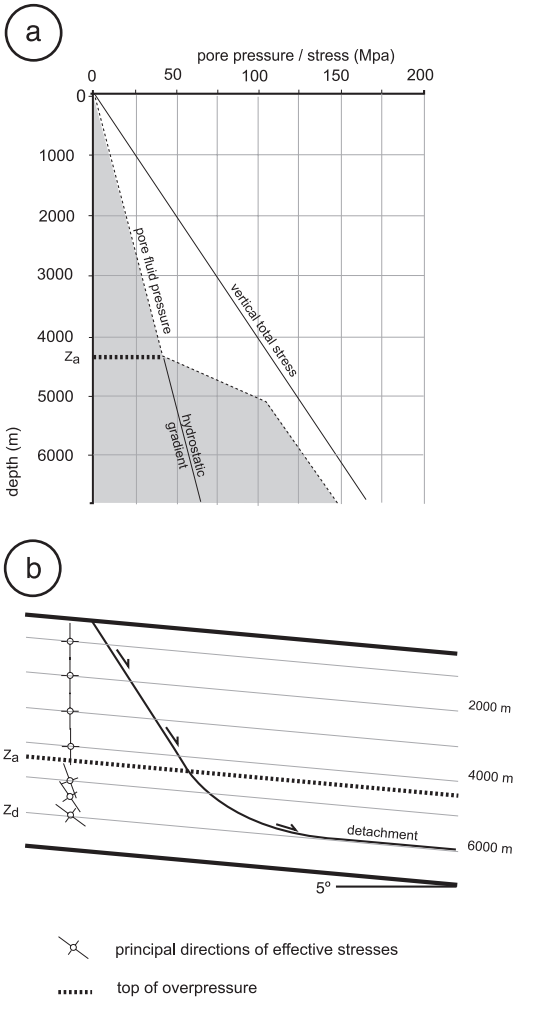

Fig. 8. Nonlinear profiles of pore fluid pressure and their mechanical consequences. Slope of pressure profile increases across less permeable layers and decreases across more permeable layers (a). Theory of gravitational gliding (Crans et al., 1980; Mandl and Crans, 1981) predicts reorientations of principal stresses and faults (b).

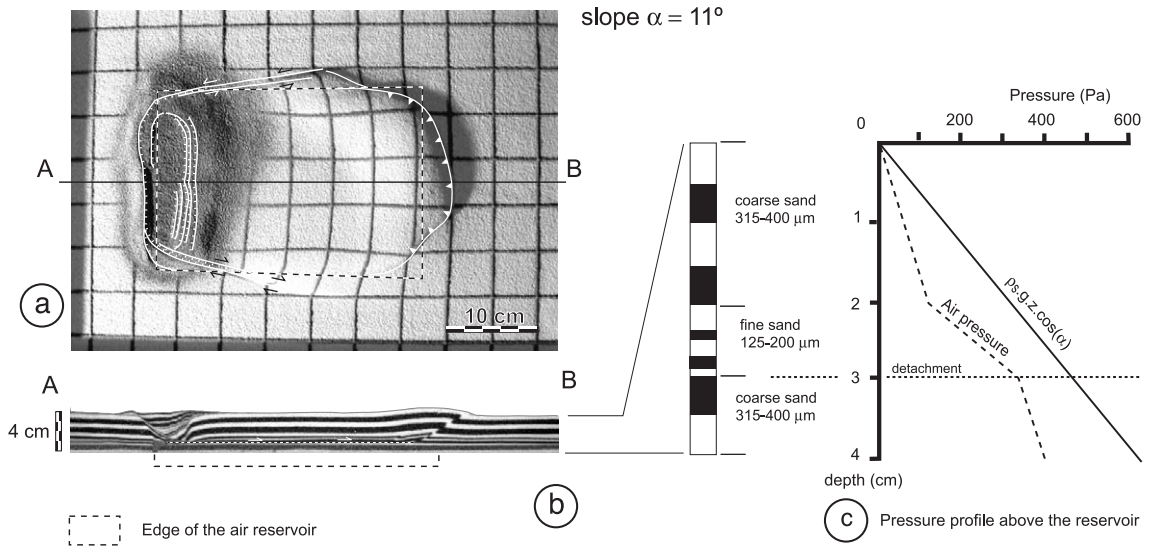

Fig. 9. Gravitational gliding in a sloping sand pack as a result of seepage forces in an area of fluid overpressure. For apparatus, see Fig. 6. Sand pack is longer and wider than pressure chamber (a). It consists of three layers of different grain sizes and permeabilities (b). After tilting apparatus and sand pack to right through 11°, basal fluid pressure was increased in steps. When it reached 400 Pa, gliding occurred on basal detachment in area above pressure chamber. Basal detachment was at a depth where calculated pressure was closest to lithostatic (c).

compensate for the lack of overburden and avoid an explosive formation of gas chimneys. On increasing the air pressure once more, the slide advanced another step. We were able to repeat this procedure several times. At the end of the experiment, serial sections showed that the slide had detached sharply at the base of the confining layer, where the air pressure was closest to lithostatic, as occurred in previous experiments on thrust belts (Cobbold et al., 2001). Normal faults and reverse faults had listric shapes, curving progressively out of the detachment, as predicted by the theoretical model of Crans et al. (1980).

5.2. Horizontal sedimentary sequence with lateral variation of fluid pressure

In previous experiments, air flowed in a direction perpendicular to the surface of a sloping sand pack, so that seepage forces influenced the orientations of principal stresses and faults. Lateral variations in fluid pressure within horizontal sand packs can produce similar effects.

We have done some extensional tests involving complex pressure distributions in horizontal sand packs (Fig. 10). We used the set-up previously described, where a horizontal sand pack rests on two overlapping sieves. However, in this instance, we placed the pressure chamber so that one of its edges was under the strip of overlapping sieves. On displacing one sieve over the other, we obtained a velocity discontinuity. A pair of conjugate faults appeared at the discontinuity, forming a rift valley at the surface. The faults were strongly listric, one of them passing from a normal fault at the surface to a reverse fault at depth. We calculated the pressure distribution in the sand by solving Darcy's equations for fluid flow in two dimensions, using a finite-difference method. Notice the strong horizontal gradient of fluid pressure in the area of faulting. In the experiments, if the principal effective compression bisected the dihedral angle between faults, it had a strongly curved trajectory. This is compatible with the sense and orientation of seepage forces in the numerical calculation.

Many authors have addressed the formation of listric faults (Price, 1977; Shelton, 1984; Bradshaw and Zoback, 1988). Shelton (1984) has summarized existing theories. It is a common observation that faults flatten into overpressured sediment. Bradshaw

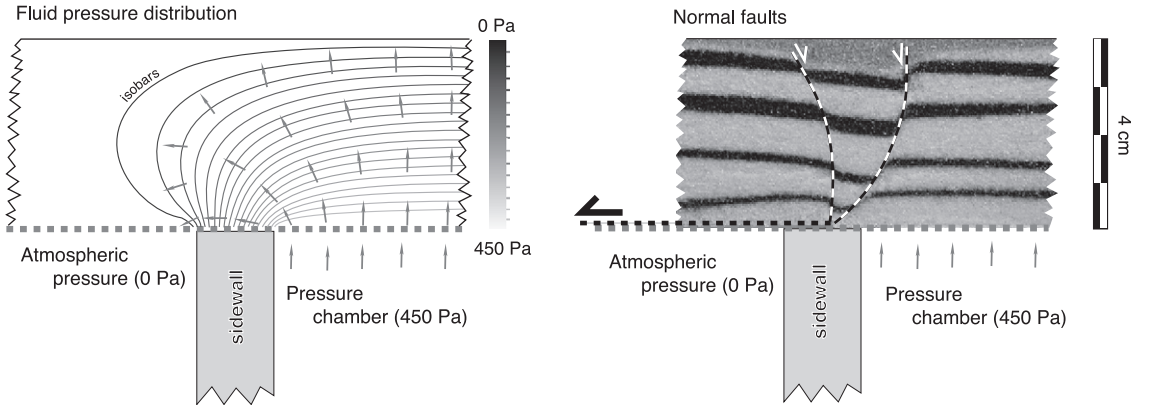

Fig. 10. Formation of curved extensional faults in area of complex overpressure gradients within a sand pack. For apparatus, see Fig. 6. Sidewall of pressure chamber was beneath centre of sand pack, where basal sieves overlapped. Air pressure was 450 Pa in chamber. Air flowed upward and sideways in response to complex pressure gradients within the sand, investigated by numerical modelling (left). Sliding of one sieve over another created velocity discontinuity. Extensional faults formed above the discontinuity (right). Faults and inferred principal compression curved from base to top of sand pack as a result of seepage forces.

and Zoback (1988) explained this observation in terms of stress refraction between layers of contrasting viscosities. Although Mandl and Crans (1981) had previously developed a model of gravitational gliding, in which seepage forces resulted in listric faults, it seems to have found little acceptance. We hope that our experiments will remedy that situation.

6. Mohr's stress circles for effective stress and total stress

On a plot of shear stress versus normal stress, Mohr's stress circle represents the state of stress at a point P in the material. According to von Terzaghi's principle ($\sigma'_n = \sigma_n - P_f$; $\tau' = \tau$ in all directions), effective stress and total stress plot as circles of the same radius, offset along the horizontal axis by an amount equal to pore fluid pressure.

Starting with total stresses, it is common to calculate effective stresses by assuming a hydrostatic state for the pore fluid. If total stresses are constant, any variation dP_f in fluid pressure then implies a shift of the effective stress circle along the horizontal axis.

Whereas constant total stress may be a reasonable assumption in some circumstances, such as triaxial laboratory tests, its validity may be questionable in natural examples, where there are fluid overpressures. Because of seepage forces, a variation dP_f in fluid pressure can change all of the total stresses (both normal and shear stresses).

To illustrate this situation, we will consider the state of stress in an isotropic elastic porous medium, formulating constitutive equations in terms of effective stress.

6.1. Horizontal sedimentary sequence

Consider a horizontal sedimentary sequence that suffers no horizontal strain ($\varepsilon_x = 0$). The total vertical stress is $\sigma_z = \rho_b g z$. The fluid overpressure gradient is purely vertical. The horizontal and vertical effective stresses are σ'_x and σ'_z, respectively. For a compressible elastic material, they are proportional:

$$\sigma'_x = K\sigma'_z \tag{19}$$

Here, $K = \nu/(1-\nu) < 1$ for plane strain, where ν is Poisson's ratio.

Because the gradient of total vertical stress is constant, any time variation dP_f in fluid pressure induces variations in both vertical and horizontal effective stresses:

$$d\sigma'_z = -dP_f; d\sigma'_x = -K dP_f \tag{20}$$

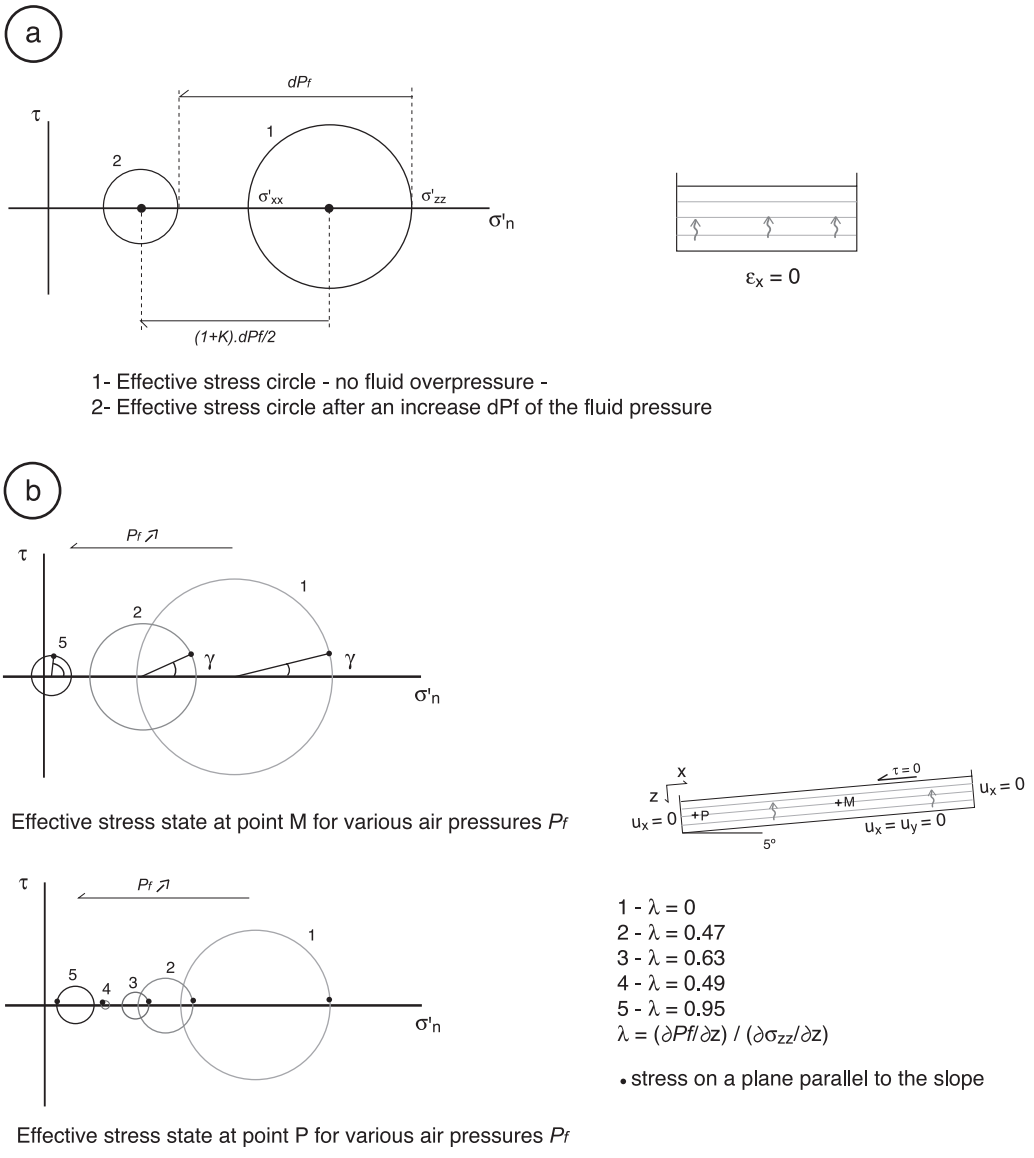

Fig. 11. Mohr's stress circles for a sedimentary sequence, horizontal or inclined. Exact solution for a poroelastic medium in plane strain with no horizontal extension (a) yields circles for effective stress that differ depending on value of overpressure at base of sequence. Notice that radius of circle changes, as well as its position along horizontal axis. Numerical model of elastic deformation and air flow in an inclined sequence gives similar results. For increasing fluid overpressures, radius of effective stress circle increases and principal stresses rotate (b).

The total horizontal stress also varies:

$$\mathrm{d}\sigma_x = (1 - K)\mathrm{d}P_\mathrm{f} \tag{21}$$

In such a system, any variation in fluid pressure implies a change in the radius of Mohr's stress circle (Fig. 11a). The effective shear stresses are invariant on horizontal and vertical planes, but they vary on all others. Such a coupled variation in pore pressure and stress has been found in many sedimentary basins and oil fields. Hillis (2001), summarising data from various basins, found that K ranged

from 0.2 to 0.7, and debated possible mechanisms of failure.

Similar stress calculations can be done with other constitutive laws, such as a Mohr–Coulomb criterion without cohesion, where $K=(1-\sin\phi)/(1+\sin\phi)$, or a plasticity law, where $K=1$. For further discussion and references, see Hillis (2001).

6.2. Sloping sedimentary sequence

For a sloping sedimentary sequence, it is unrealistic to assume no lateral strain. We have calculated, by a two-dimensional numerical method, the effect of fluid overpressure parallel to slope on the state of stress in an inclined elastic porous body. We chose a shape like our sand experiments. The model is, therefore, 30 cm long and 4 cm thick. The slope is 7°. The fluid is air. The boundary conditions on the displacements are $u_x=0$ on the walls and $u_x=u_z=0$ at the base (Fig. 11b). The effective stresses are calculated for plane strain. The fluid pressure is from Darcy's law, assuming flow perpendicular to the slope. We assume a steady state, so that the stress calculation does not depend on the fluid pressure calculation (Iverson and Reid, 1992).

We illustrate the results by Mohr circles for two material points and various rates of fluid flow (Fig. 11b). Point M is in the middle of the model, whereas point P is close to its downhill boundary. An increase in fluid pressure has several effects.

1. As before, the radius of the Mohr circle diminishes.
2. The stress tensor rotates (γ varies).
3. Near the downhill boundary, the deviatoric stress (radius of the circle) reaches a minimum and increases again. The principle stress σ_1' is then closer to x than to the vertical, so that this part of the model begins to compress.

In this model, the reorientation of principal stresses (Mandl and Crans, 1981) is due, not to limitations on stress values at yield, but to the fluid pressure gradient, which acts as a body force (seepage force).

7. Conclusions

By a series of very simple experiments involving fluid flow through sand, we have demonstrated the action of a fluid pressure gradient in a porous medium. We have verified von Terzaghi's principle in shear tests that have allowed us to describe accurately the behaviour of a grade of sand that has been used in analogue experiments. We have also demonstrated a silo effect. In extensional experiments, we have measured an increasing coefficient of friction for stresses smaller than 30 Pa. This result is in contradiction with previous work. We have also demonstrated reorientation of stresses in various experiments and have partly verified the model of Mandl and Crans (1981) for growth faulting and gravity gliding. We hope that this review will clarify some of the complications that fluid overpressures and seepage forces may impose on stress distributions in various tectonic settings.

Acknowledgements

PRC acknowledges illuminating discussions with Florian Lehner in Strasbourg and in Paris.

Appendix A. Errors due to sidewall friction during shear tests on sand

Dry sand has been widely used in analogue modelling to represent brittle rock in the upper crust. Most workers have assumed that cohesion of sand is negligible and that the angle of internal friction is close to 30°. Some experimenters have attempted to measure these parameters.

In shear tests on Fontainebleau sand, Krantz (1991) obtained extrapolated cohesions of 300 Pa for poured sand and 520 Pa for sprinkled sand, and a frictional coefficient between 0.58 for poured sand and 1.00 for sprinkled sand. To experimenters who know that dry sand is little able to support vertical relief, the cohesion measured by Krantz may seem surprisingly large (see Discussion in Richard and Krantz, 1991).

Schellart (2000) attributed large values of cohesion to errors in extrapolating failure envelopes because of a lack of data for normal stresses smaller than 600 Pa. He, therefore, did a further series of shear tests for normal stresses of 50–900 Pa using a smaller cylinder. For several kinds of granular material, he ob-

tained failure envelopes in two parts: a curved part near the origin for normal stresses smaller than a critical value (250–400 Pa), and a linear part for larger normal stresses. From independent measurements of fault dips, he, nevertheless, found no dependence of μ on σ_n. To reconcile this invariant μ with curvature of a failure envelope near the origin, he concluded, erroneously, that cohesion was a function of normal stress.

Cobbold and Castro (1999) did further shear tests for normal stresses ranging from 300 to 1600 Pa. They obtained an extrapolated cohesion of 85 Pa and a coefficient of internal friction of 0.57. The material was Fontainebleau sand. They sieved it, retaining the fraction with grain sizes between 0.200 and 0.315 mm. To obtain samples with reproducible properties, Cobbold and Castro fluidised them with air and then compacted them by tapping. The authors noted that internal friction was small and close to Krantz's values for poured sand, despite differences in the manner of preparing the sand packs.

In summary, tests on sand have produced conflicting results. Krantz's values of cohesion seem too high and the curved failure envelopes of Schellart are not compatible with the dips that he measured on faults. We believe that most of these problems result from sidewall friction in the test cylinders.

Jansen's model of sidewall friction (the silo effect)

To obtain a failure envelope, we need the shear stress and normal stress acting on a fault plane. For basal shear in a shear box, we measure a shear load and divide it by the basal area, whereas the normal stress we deduce from the weight and thickness of the sand:

$$\tau = mg/A \tag{A0}$$

$$\sigma_n = \rho_s g h \tag{A1}$$

Here, m is the mass of the shear load, A the area of the fault surface, h the thickness of the sand pack, ρ_s the sand density and g the acceleration of gravity.

Sidewall friction, between the sand and the cylinder, may partly counteract the weight of the sand, reducing the normal stress. If so, Eq. (A1) no longer holds. Krantz (1991) and Cobbold and Castro (1999) did not refer to this kind of problem, although they were certainly aware of it, and Schellart (2000) considered it as negligible without giving any proof.

Jansen (1895) derived a simple mechanical model to account for sidewall friction at the edges of a silo, hopper, or container of granular material. He assumed that vertical stress σ_v automatically results in a proportional horizontal stress, σ_h:

$$\sigma_h = K\sigma_v$$

Here, K is a stress ratio, which depends on the packing of the granular material. For close packing of spheres, $K = 0.58$ (Duran, 1997).

Consider a cylindrical container full of sand (Fig. A1). The balance of forces across a horizontal element of thickness dz gives:

$$A\mathrm{d}\sigma_v + K\mu_s P\sigma_v \mathrm{d}z = \rho_s g A \mathrm{d}z \tag{A2}$$

Here, A is the cross-sectional area of the sand, P its perimeter, μ_s the coefficient of sidewall friction and ρ_s the sand density. The second term in the equation is the frictional force between sand and container.

By integrating Eq. (A2), we obtain:

$$\sigma_v.\exp(K\mu_s Pz/A) = \rho_s gA/(PK\mu_s)\exp(K\mu_s Pz/A) + C \tag{A3}$$

Here, C is a constant. For boundary conditions, $\sigma_v = 0$ at $z = 0$, the equation reduces to:

$$\sigma_v = \rho_s gD/(4K\mu_s)(1 - \exp(-4K\mu_s z/D)) \tag{A4}$$

Here, D is the diameter of the cylinder.

For shallow depths, the profile of vertical stress is close to a straight line of slope $\rho_s g$ (Fig. A1a). Further down, the vertical stress tends asymptotically to a constant value. From that depth on, sidewall friction totally counteracts the additional weight of sand.

For a given cylinder, the vertical stress depends on μ_s, in other words, on the material of the container. Krantz (1991) used a cylinder made of glass, whereas the cylinders used Cobbold and Castro (1999) and Schellart (personal communication, 2002) were made of transparent plastic material. To determine the coefficient of friction between sand and plastic material, we

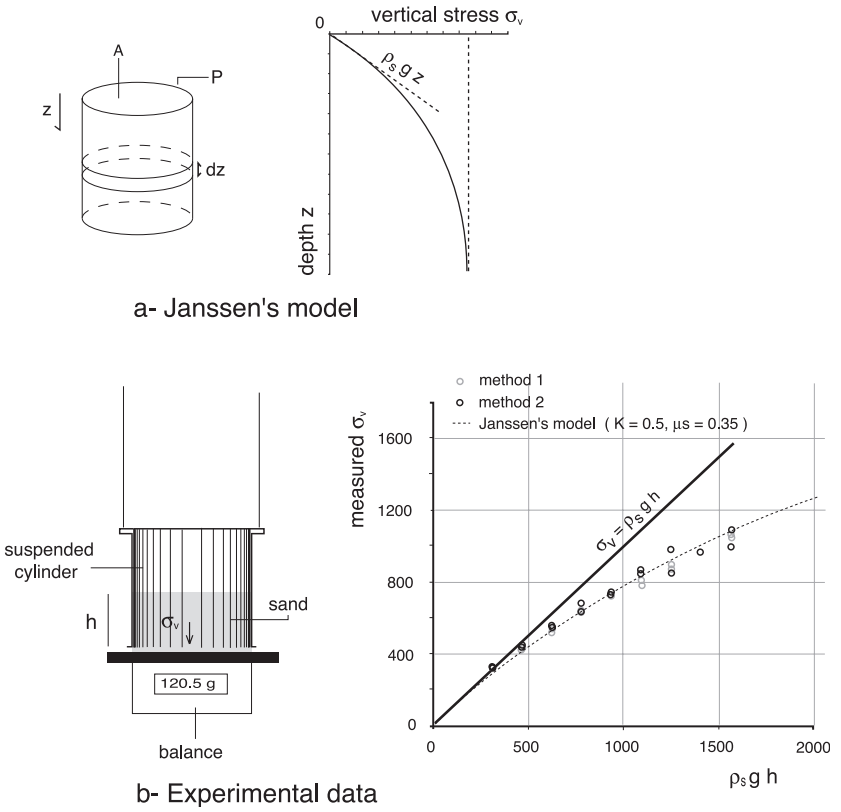

Fig. A1. Testing Jansen's model of sidewall friction. The model applies to granular material within a container (a). Vertical stress decreases exponentially with depth as a result of sidewall friction. For tests, sand was in cylindrical container suspended above balance (b). For two different methods of preparing sand pack (see text), results were similar (right). Measured weight of sand was systematically smaller than true weight. Jansen's model fits data well for sidewall friction of $\mu_s = 0.35$, which was measured independently, and stress ratio of $K = 0.5$, which is close to theoretical predictions.

did some additional shear tests (Fig. A2). We suspended a cylinder containing sand above a transparent plastic sheet, resting on a balance. Then we applied an increasing shear load until sand and container slid over the plastic sheet. We tested three grades of Fontainebleau sand, having grain sizes of (1) less than 0.5 mm, (2) between 0.315 and 0.400 mm and (3) between 0.200 and 0.315 mm. The coefficient of sliding friction, μ_s, was between 0.3 and 0.4.

To quantify sidewall friction in a shear apparatus, we placed a given weight of sand in a suspended transparent plastic cylinder, 9 cm in diameter (Fig. A1b). We used Fontainebleau sand with a grain size between 0.200 and 0.315 mm and we tested two methods of preparing samples. In Method 1, the cylinder hung 0.2 mm above a balance; a known mass of sand was poured into it from a height of 10 to 20 cm; and the weight of sand supported by the balance was then recorded. In Method 2, the cylinder rested on the balance; the sand was slowly sprinkled into it; and the container was then suspended.

The results of these tests are diagnostic of sidewall friction. Regardless of the method used to prepare samples, Jansen's model (Eq. (A4)) fits the data well. The best-fit exponential curve is for $\mu_s = 0.35$ and $K = 0.5$. These parameters seem to be realistic. The coefficient of friction is close to that determined in our shear tests.

The same experiments were done with a cylinder made of glass. The best-fit exponential curve was for $\mu_s = 0.1$ and $K = 0.5$. This shows that

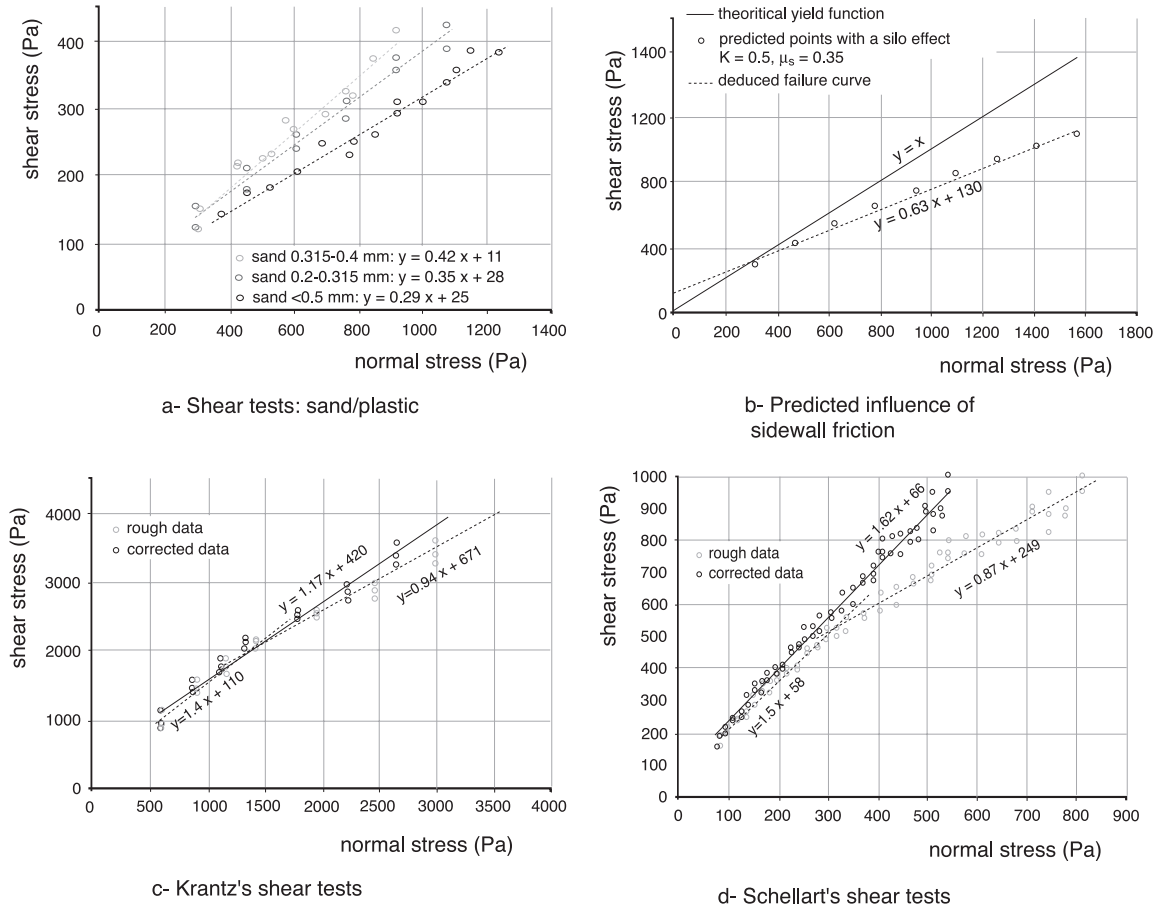

Fig. A2. Plots of shear stress versus normal stress for various tests not involving fluid flow. Tilting of sand pack lying on transparent plastic sheet resulted in shearing at contact (a). For various grades of sand, yield envelopes are linear and no correction is necessary. For shear tests where sand lies in plastic container, sidewall friction influences results. Assuming that sand has linear yield envelope and no cohesion (full line), Jansen's model predicts that measurements will deviate (b), so that best-fit straight line (dotted) will indicate small coefficient of internal friction (0.63) and large cohesion (130 Pa). For shear tests by Krantz (c) and Schellart (d), raw data indicate nonlinear envelopes, whereas corrected data indicate linear ones. Corrected values of cohesion are much smaller than uncorrected values, whereas corrected values of internal friction are larger than uncorrected values.

friction between sand and glass was much smaller than that between sand and transparent plastic material. Glass is, therefore, preferable for reducing boundary friction.

Influence of sidewall friction on measurements of internal friction and cohesion

By neglecting boundary effects during shear tests, an experimenter may overestimate the normal stress that acts on the failure surface.

One way of illustrating this effect is to assume that we know the true properties of a given batch of sand and then to calculate what the apparent properties will be if we mistakenly neglect sidewall friction. Consider a sand which fails when $\tau = \sigma_n$, so that $\mu = 1$ and $c = 0$. Now consider shear tests in the cylinder used by Cobbold and Castro (1999), for heights of sand ranging between 2 and 10 cm. Because of errors in the estimation of normal stress, the failure envelope will be incorrect (Fig. A2b). The best-fit straight line to the incorrect data gives $\mu = 0.63$ and $c = 130$

Pa. Thus, by neglecting sidewall friction, the experimenter may overestimate cohesion and underestimate internal friction.

Correcting the results of Krantz and Schellart

In the shear tests of Krantz (1991), the internal diameter, D, of the cylinder was 14 cm, whereas, in those of Schellart (2000), it was 3.2 cm. The apparent failure envelopes are curved (Fig. A2). Following Schellart, we consider these curves in two parts and plot two straight lines, a steep one for small normal stresses and a gentle one for large normal stresses. The steep lines have slopes of 1.4 (for Krantz's data) and 1.5 (for Schellart's data). The gentle lines have slopes of 0.94 and 0.87, respectively. For Krantz's data, steep and gentle lines intersect at $\sigma_n = 1500$ Pa, which is equivalent to a height, h, of about 8 cm of sand in the cylinder. Hence, $r = h/D = 0.57$. For Schellart's data, the intersection is at about 300 Pa ($h = 1.8$ cm), so that $r = 0.56$. The similar values of r given by Schellart's data and Krantz's data indicates that the curvature of the failure envelopes is due to sidewall friction and does not represent the mechanical behaviour of the sand.

By using Eq. (A4), we can apply a correction to the normal stresses. For both data sets, the corrected points follow straight lines better than do the uncorrected points. For Krantz's data, the corrected coefficient of friction is 1.17 and the corrected cohesion is 420 Pa (instead of 520 Pa). For Schellart's data, the corrected values are $\mu = 1.6$ and $c = 66$ Pa. The former value is close to the slopes of straight lines fitted to uncorrected data, where $r < 0.56$. It also agrees with the results of extensional tests.

In conclusion, sidewall friction has nonnegligible effects, and shear tests should be done where $r < 0.6$. Even then, Jansen's model provides a useful correction to the data.

Boundary effects for shear tests involving a fluid flow

Using the apparatus previously described (Fig. 3), we have estimated the effect of sidewall friction for shear tests involving vertical fluid flow. The tests were for sand thicknesses of 2–7 cm and for three values of λ. On plots of normal stress versus theoretical effec-

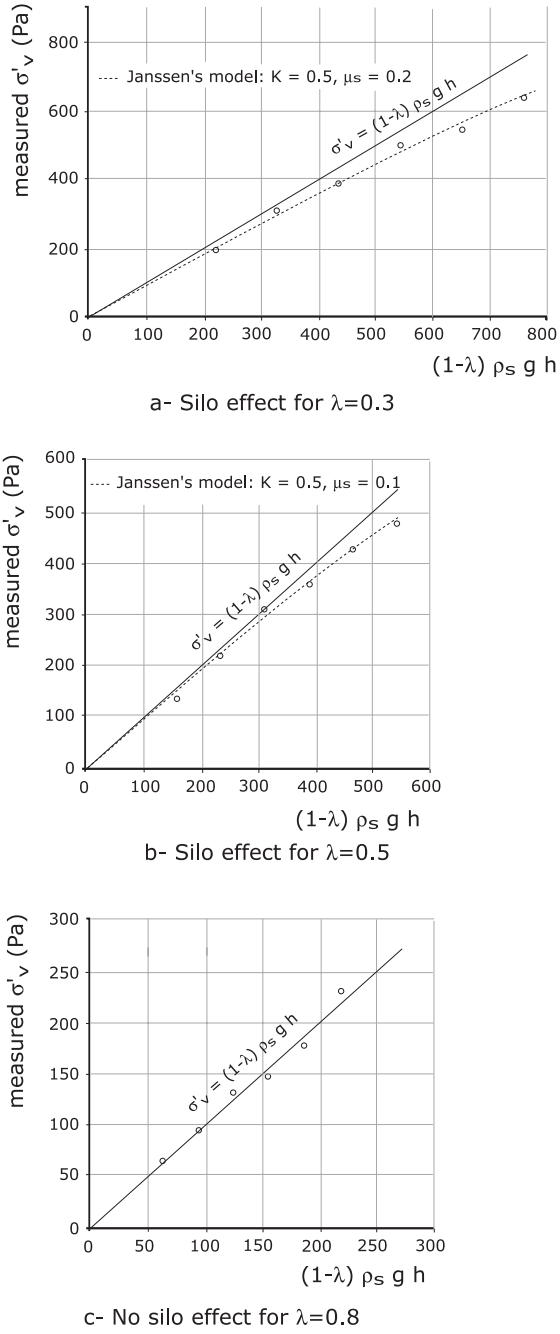

Fig. A3. Effects of sidewall friction during fluid flow. Plots are for measured effective normal stress as function of theoretical effective normal stress. Jansen's model fits data well. Effects of sidewall friction are inferred for small values of fluid ratio, λ, but are negligible for large values ($\lambda = 0.8$).

tive stress, $\sigma'_n = (1-\lambda)\rho_s g h$, we have fitted the best exponential curve to the data (Fig. A3). In so doing, we have assumed a constant K because the packing visibly did not change. As λ increases, the estimated values of μ_s decreases. For $\lambda = 0.8$, the data seem to indicate no frictional effect.

Variation of μ_s does not necessarily imply a decrease in frictional resistance between sand and plastic container. We think rather that sidewall friction can oppose not only the weight of the sand, but also the upthrust provided by migrating air. We speculate that these two frictional forces, which have opposite senses, can cancel each other for $\lambda = 0.8$.

References

Biot, M.A., 1941. General theory of three-dimensional consolidation. Journal of Applied Physics 12, 155–164.

Birch, F., 1961. Role of fluid pressure in mechanics of overthrust faulting: dicussion. Geological Society of America Bulletin 72, 1441–1451.

de Boer, R., 2000. Theory of Porous Media. Highlights in the Development and Current State. Springer, Berlin. 618 pp.

Bradshaw, G.A., Zoback, M.D., 1988. Listric normal faulting, stress refraction, and the state of stress in the Gulf Coast basin. Geology 16, 271–274.

Byerlee, J., 1992. The change in orientation of subsidiary shears near faults containing pore fluid under high pressure. Tectonophysics 211, 295–303.

Cobbold, P.R., Castro, L., 1999. Fluid pressure and effective stress in sandbox models. Tectonophysics 301, 1–19.

Cobbold, P.R., Duran, S., Mourgues, R., 2001. Sandbox modelling of thrust wedges with fluid assisted detachments. Tectonophysics 334, 245–258.

Crans, W., Mandl, G., Haremboure, J., 1980. On the theory of growth faulting: a geomechanical delta model based on gravity sliding. Journal of Petroleum Geology 2, 265–307.

Dahlen, F.A., 1984. Noncohesive critical Coulomb wedges: an exact solution. Journal of Geophysical Research 89 (B12), 10125–10133.

Dahlen, F.A., 1990. Critical taper model of fold-and-thrust belts and accretionary wedges. Annual Reviews of Earth and Planetary Science 18, 55–99.

Dahlen, F.A., Suppe, J., Davis, D., 1984. Mechanics of fold-and-thrust belts and accretionary wedges: cohesive Coulomb theory. Journal of Geophysical Research 89 (B12), 10087–10101.

Davis, D., Suppe, J., Dahlen, F.A., 1983. Mechanics of fold-and-thrust belts and accretionary wedges. Journal of Geophysical Research 88 (B2), 1153–1172.

Duran, J., 1997. Sables, poudres et grains: Introduction à la physique des milieux granulaires. Eyrolles Sciences, Paris. 251 pp.

Fillunger, P., 1913. Der Auftrieb in Talsperren. Österreichische Wochenschrift für den öffentlichen Baudienst, 19, 532–556, 567–570.

Fillunger, P., 1914. Neuere Grundlagen für die statische Berechnung von Talsperren. Zeitschrift des Österreichischen Ingenieur und Architekten Vereines 23, 441–447.

Garg, S.K., Nur, A., 1973. Effective stress laws for fluid-saturated porous rock. Journal of Geophysical Research 78 (26), 5911–5921.

Garven, G., 1995. Continental scale groundwater flow and geologic processes. Annual Reviews of Earth and Planetary Science 89, 89–117.

Handin, J., Hager, R.V., Friedman, J.R.M., Feather, J.N., 1963. Experimental deformation of sedimentary rocks under confining pressure: pore pressure tests. American Association of Petroleum Geologists Bulletin 47, 717–755.

Hillis, R.R., 2001. Coupled changes in pore pressure and stress in oil field sedimentary basins. Petroleum Geosciences 7, 419–425.

Hobbs, B.E., Means, W.D., Williams, P.F., 1976. An Outline of Structural Geology. Wiley, New York. 571 pp.

Hubbert, M.K., Willis, D.G., 1957. Mechanics of hydraulic fracturing. Transactions of the American Institute of Mechanical Engineers 210, 153–168.

Hubbert, M.K., Rubey, W.W., 1959. Role of fluid pressure in mechanics of overthrust faulting. Geological Society of America Bulletin 70, 115–166.

Iverson, R., 1991. Can magma-injection and groundwater forces cause massive landslides on Hawaiian volcanoes? Journal of Volcanology and Geothermal Research 66, 295–308.

Iverson, R., Major, J.J., 1986. Groundwater seepage vectors and the potential for hillslope failure and debris flow mobilization. Water Resources Research 22, 1543–1548.

Iverson, R., Reid, M., 1992. Gravity-driven groundwater flow and slope failure potential: 1. Elastic effective-stress model. Water Resources Research 28, 925–938.

Jansen, H.A., 1895. Versuche über Getreidedruck in Silozellen. Zeitschrift des Vereiner Deutscher Ingenieure 39, 1045–1049.

Koyi, H., 1997. Analogue modelling: from a qualitative to a quantitative technique—a historical outline. Journal of Petroleum Geology 20, 223–238.

Krantz, R.W., 1991. Measurements of friction coefficients and cohesion for faulting and fault reactivation in laboratory models using sand and sand mixtures. Tectonophysics 188, 203–207.

Laubsher, H.P., 1960. Role of fluid pressure in mechanics of overthrust faulting. Geological Society of America Bulletin 71, 611–628.

Lehner, F.K., 1986. Comments on "noncohesive critical Coulomb wedges: an exact solution" by F.A. Dahlen. Journal of Geophysical Research 91 (B1), 793–796.

Mandl, G., 1988. Mechanics of tectonic faulting: models and basic concepts. Developments in Structural Geology. Elsevier, Amsterdam. 407 pp.

Mandl, G., Crans, W., 1981. Gravitational gliding in deltas. In: McClay, K.R., Price, N.J. (Eds.), Thrust and Nappe Tectonics. Geological Society of London Special Publication, vol. 9, pp. 41–54.

Mello, U.T., Pratson, L.F., 1999. Regional slope stability and slope-failure mechanics from the two-dimensional state of stress in an infinite slope. Marine Geology 154, 339–356.

Moore, W.L., 1961. Role of fluid pressure in overthrust faulting: a discussion. Geological Society of America Bulletin 72, 1581–1594.

Nur, A., Byerlee, J.D., 1971. An exact effective stress law for elastic deformation of rock with fluids. Journal of Geophysical Research 76 (B6), 6414–6419.

Oliver, J., 1986. Fluids expelled tectonically from orogenic belts: their role in hydrocarbon migration and other geological phenomena. Geology 14, 99–102.

Orange, D., Breen, N., 1992. The effect of fluid escape on accretionary wedges: 2. Seepage force, slope failure, headless submarine canyons, and vents. Journal of Geophysical Research 97 (B6), 9277–9295.

Price, N.J., 1977. Aspect of gravity tectonics and the development of listric faults. Journal of the Geological Society of London 133, 311–327.

Price, N.J., Cosgrove, J.W., 1990. Analysis of Geological Structures. Cambridge Univ. Press, Cambridge. 502 pp.

Ramsay, G., Huber, M.I., 1983. The Techniques of Modern Structural Geology, vols. 1 and 2. Academic Press, London. 700 pp.

Rice, J.R., 1975. On the stability of dilatant hardening for saturated rock masses. Journal of Geophysical Research 80 (11), 1531–1536.

Rice, J.R., Cleary, M.P., 1976. Some basic stress diffusion solutions for fluid-saturated elastic porous media with compressible constituents. Reviews of Geophysics and Space Physics 14, 227–241.

Richard, P., Krantz, R.W., 1991. Experiments on fault reactivation in strike-slip mode. In: Cobbold, P.R. (Ed.), Experimental and Numerical Modelling of Continental Deformation. Tectonophysics, vol. 188, pp. 117–131.

Robin, P.Y.F., 1973. Note on effective pressure. Journal of Geophysical Research 78 (14), 2434–2437.

Rudnicki, J.W., 1984. Effects of dilatant hardening on the development of concentrated shear deformation in fissured rock masses. Journal of Geophysical Research 89 (B11), 9259–9270.

Schellart, W.P., 2000. Shear test results for cohesion and friction coefficients for different granular materials: scaling implications for their usage in analogue modelling. Tectonophysics 324, 1–16.

Shelton, J.W., 1984. Listric normal faults: an illustrated summary. American Association of Petroleum Geologists Bulletin 68, 801–815.

Sibson, R.H., 2000. Fluid involvement in normal faulting. Journal of Geodynamics 29, 469–499.

Strayer, L.M., Hudleston, P.J., Lorig, L.J., 2001. A numerical model of deformation and fluid-flow in an evolving thrust wedge. Tectonophysics 335, 121–145.

von Terzaghi, K., 1923. Die Berechnung der Durchlässigkeitsziffer des Tones aus dem Verlauf der hydrodynamischen Spannunggersheinungen. Sitzungsberichte der Akademie der Wissenschaften in Wien, mathematischnaturwissenshftliche Klasse, Abteilung IIa 132, 125–138.

Willis, S., Buck, W.R., 1997. Stress-field rotation and rooted detachment faults: a Coulomb failure analysis. Journal of Geophysical Research 102 (B9), 20503–20504.